Fourier Optics for the Analysis of Distributed Absorbers Under THz Focusing Systems

Llombart, Nuria; Blázquez, Beatriz; Freni, Angelo; Neto, Andrea

DOI
10.1109/TTHZ.2015.2439511

Publication date
2015

Document Version
Accepted author manuscript

Published in
IEEE Transactions on Terahertz Science and Technology

Fourier Optics for the Analysis of Distributed Absorbers Under THz Focusing Systems

Nuria Llombart, *Senior Member, IEEE*, Beatriz Blázquez, Angelo Freni, *Senior Member, IEEE*, and Andrea Neto, *Senior Member, IEEE*

***Abstract*—An analytical spectral model able to accurately and efficiently characterize absorbers distributed in the focal plane of focusing THz systems is presented. The model is obtained by using a Fourier optics representation of the electromagnetic field in the focal plane in conjunction with a recently developed equivalent network representation for the interaction of plane waves with distributed absorbers. The model is validated by comparisons with numerical full-wave simulations. Finally, the model is used to design a few architectures based on lens-coupled Kinetic Inductance Detectors (KIDs), which show high absorption efficiency over a large bandwidth.**

***Index Terms*—Focusing systems, Fourier optics, THz absorbers.**

I. Introduction

THE next generation of terahertz (THz) instruments for space imaging requires arrays of thousands of detectors located in the focal plane of a telescope [1]. Kinetic Inductance Detectors (KIDs) [2], [3] are microwave superconducting resonators that can relate the received THz power to changes in the microwave resonance frequencies. They have been proposed for space imaging because of their unprecedented intrinsic read-out potential, which derives from the possibility of using frequency multiplexing techniques. Arrays with $>$ 20 K elements have been recently demonstrated [4].

KIDs can be coupled to the incoming THz radiation either via absorbers [5]–[7] or antennas [8]. In the past, absorbers have been used directly as free-standing arrays in the focal plane of a reflector system [5], [7]. However, external coupling mechanisms (i.e., horns or lenses) are currently under investigation to improve the sampling efficiency and to reduce the mutual coupling between KIDs [6], [9]. Moreover, absorbers placed in the interface between silicon and air have the potential to achieve larger frequency bandwidths [10].

Manuscript received November 06, 2014; revised May 04, 2015; accepted May 12, 2015. Date of publication July 08, 2015; date of current version July 16, 2015. This work was supported as part of a collaborative project, SPACEKIDS , under Grant 313320 provided by the European Commission under Theme SPA. 2012.2.2-01 of Framework Programme 7, and by the ERC starting grants ERC-2011-STG GRANT AAATSI 278794.

N. Llombart, B. Blazquez, and A. Neto are with the Terahertz Sensing Group, Technical University of Delft, Delft, 2628 CD, the Netherlands (e-mail: B.BlazquezValles@tudelft.nl).

A. Freni was with Terahertz Sensing Group, Technical University of Delft, Delft, 2628 CD, the Netherlands, on leave from the Department of Electronic Engineering, University of Florence, 50121, Florence, Italy.

Color versions of one or more of the figures in this paper are available online at http://ieeexplore.ieee.org.

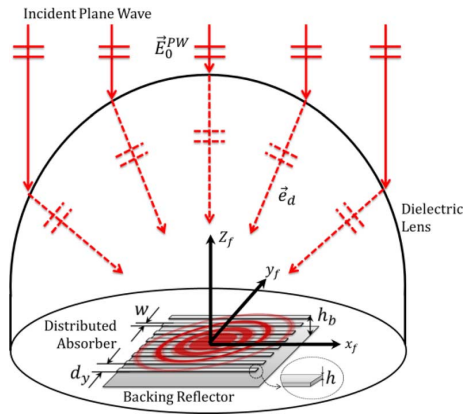

Fig. 1. Linearly polarized absorber placed at the focal plane of a focusing system.

While the properties of antenna coupled KIDs can be studied in transmission or in reception, due to reciprocity, the absorbers configuration can only be studied in reception. In view of this, the analysis of the absorbed based detectors is typically carried out by full wave simulations under normal plane wave incidence [5], [11]. However, resorting to a single pane wave incidence, the actual coupling to the focusing system, which occurs via a finite spectrum of plane waves, is typically not well described. The single plane wave procedure is accurate for large Focal Distance-to-Diameter ratio (F/D) (i.e., focusing systems where the focal field is the result of a small angular spectrum) typical scenario for instruments with free-standing absorbers in the focal plane of a telescope. However, in case of coupling through lenses which are characterized by smaller F/D ratios, the standard normal plane wave incidence is not appropriate any more.

In this paper, the coupling between focusing systems and linearly polarized absorbers (see Fig. 1), embedded in a generic multi-layer dielectric structure, is investigated by using an analytical spectral model based on Fourier optics (FO) [12] coupled with an equivalent network representation presented in [10]. The proposed method is able to analytically and efficiently characterize the power captured by distributed absorbers located under focusing systems, also with small F/D ratios, printed on a multilayer dielectric structure. An effort has been made to highlight the absorber minimum dimension for which the mentioned method provides accurate results.

Two cases are taken as reference: a free-standing absorber under a parabolic reflector and an absorber under a dielectric elliptical lens. The method shows that the power captured by free-standing absorbers varies smoothly with large F/D ratios

as expected. On the contrary, when dense lenses are present, the absorbed power shows a surprising dependence from the geometrical parameters. Even so, absorbers under dense lenses can show higher efficiencies over wide frequency bands than free-standing ones. The method is validated with full-wave time-consuming simulations.

The paper is structured as follows. In Section II, the methodology to calculate the power absorbed for a generic incident field is described. In Section III, the FO-based plane wave spectrum (PWS) for a general focusing system is obtained. Then, the field expression for two canonical geometries, parabolic reflectors and elliptical dielectric lenses, is explicitly derived in Section IV. The method is validated by comparisons with standard physical optics (PO) analysis and a full wave technique in Section V. Finally, some absorber designs to be used in KIDs are presented in Section VI. The conclusions are finally provided in Section VII.

II. Absorber Current Induced by a General Field Configuration

KIDs based on absorbers can be modeled as a series of parallel and infinitely long absorbing strips with a width w, [10]. The strips are periodically and tightly arranged, with period $\boldsymbol{d_y}$, to guarantee that the fundamental Floquet wave (FW), that represents the average field, would experience an approximate resistive boundary condition. Fig. 1 shows the geometry of the absorbers hosted in the focal plane of a dielectric lens and kept at a finite distance from a backing reflector. The absorbed power can be calculated over a finite area, once the current flowing on the strips is known.

Fig. 2 shows the analytical equivalent circuit, developed in [10], that allows calculation of the current at the cross section $\boldsymbol{x}$, $\boldsymbol{i_n}(\boldsymbol{x_f}, \boldsymbol{nd_y}) = \boldsymbol{I_0}(\boldsymbol{k_{xi}}, \boldsymbol{k_{yi}})\, \boldsymbol{e^{-jk_{xi}x_f}} \boldsymbol{e^{-jk_{yi}nd_y}}$, which is induced in each of the n-th strip when the absorber is illuminated by a *direct* plane wave, $\vec{\boldsymbol{E}}_{\boldsymbol{d}}(\boldsymbol{k_{xi}}, \boldsymbol{k_{yi}})$, with a propagation vector $\vec{\boldsymbol{k}}_{\boldsymbol{i}} = \boldsymbol{k_{xi}}\widehat{\boldsymbol{x}} + \boldsymbol{k_{yi}}\widehat{\boldsymbol{y}} + \boldsymbol{k_{zi}}\widehat{\boldsymbol{z}}$. The direct field is represented in Fig. 2 as a superposition of two TM and TE impinging voltage waves of amplitude $\boldsymbol{V^+_{TM}}(\boldsymbol{k_{xi}}, \boldsymbol{k_{yi}})$ and $\boldsymbol{V^+_{TE}}(\boldsymbol{k_{xi}}, \boldsymbol{k_{yi}})$, respectively. The derivation of these TE and TM sources was also described in [10] and leads to:

$$V^+_{TM}(k_{xi}, k_{yi}) = \sqrt{d_y}\vec{E}_d(k_{xi}, k_{yi}) \cdot \widehat{\rho}, \tag{1}$$

$$\boldsymbol{V^+_{TE}}(\boldsymbol{k_{xi}}, \boldsymbol{k_{yi}}) = \sqrt{\boldsymbol{d_y}}\vec{\boldsymbol{E}}_{\boldsymbol{d}}(\boldsymbol{k_{xi}}, \boldsymbol{k_{yi}}) \cdot \widehat{\boldsymbol{\phi}}. \tag{2}$$

The solution of the equivalent network gives

$$I_0(k_{xi}, k_{yi}) = \mathrm{sinc}\left(\frac{k_{yi}w}{2}\right) \frac{E_{ix}(k_{xi}, k_{yi})}{Z(k_{xi}, k_{yi}) + \frac{R_s}{w}} \tag{3}$$

where $Z(k_{xi}, k_{yi})$ is defined in [10], R_s is the sheet resistance (Ω/sq) of the strips, and $E_{ix}(k_{xi}, k_{yi})$ represents the amplitude of the x-component of the *incident* electric field calculated at the strip position in absence of the absorber, but including any possible dielectric stratification where the absorber is embedded. This field is expressed as the voltage in A-A', superposition of the fields induced by both TE and TM direct voltage waves as in [10, eq. (14)]. Note that the *incident* field, $\vec{E}_i$, is different from the *direct* field, $\vec{E}_d$, as it accounts for the presence of possible the dielectric stratifications.

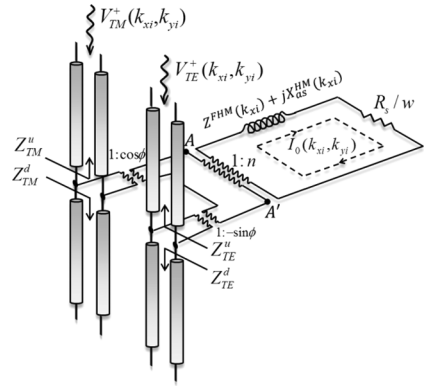

Fig. 2. Equivalent network developed in [10] for the characterization of the interaction of a plane wave with a linearly polarized absorber. Each component of the circuit is defined in [10].

When the absorber is illuminated by a generic coherent field (e.g., the field in the focal plane of a focusing system), the direct electric field $\vec{\boldsymbol{e}}_{\boldsymbol{d}}(\vec{\boldsymbol{\rho}}_{\boldsymbol{f}})$ (i.e., in absence of absorber and the stratification) can be expressed as a coherent superposition of plane waves, as follows:

$$\vec{e}_d(\vec{\rho}_f) = \frac{1}{4\pi^2}\int_{-\infty}^{\infty}\int_{-\infty}^{\infty} \vec{E}_d(k_x, k_y)\, e^{-jk_x x_f} e^{-jk_y y_f} dk_x dk_y. \tag{4}$$

In the following we will refer to $\vec{E}_f$ rather than $\vec{E}_d$, to highlight our present attention on focusing systems. This plane wave expansion is particularly useful when used in combination with the circuit of Fig. 2.

Thanks to the linearity of the system, the total current in the n-th strip of the absorber, $i_n(x_f, nd_y)$, can be expressed as the superposition of the currents induced by each of these plane waves, as follows:

$$i_n(x_f, nd_y) = \frac{1}{4\pi^2}\int_{-\infty}^{\infty}\int_{-\infty}^{\infty} I_0(k_x, k_y)\, e^{-jk_x x_f} e^{-jk_y nd_y} dk_x dk_y \tag{5}$$

where $I_0(k_x, k_y)$ is calculated by (3). The power absorbed by the strips can now be easily calculated from (5) using the sheet resistance, R_s. For a finite absorber with dimensions $L_x \times L_y$, the power absorbed can be approximated as a summation over a finite number of cells ($N = L_y/d_y$) as follows:

$$P_{\mathrm{abs}}(L_x, N) = \frac{R_s}{2w}\sum_{n=-N/2}^{N/2}\int_{-L_x/2}^{L_x/2} |i_n(x_f, nd_y)|^2 dx_f. \tag{6}$$

Expressions (5) and (6) highlight that, the coherent summation of the current induced by each of the plane waves is needed to evaluate the total power absorbed. In some cases this coherent summation operation can be simplified. That is, if the array is very well sampled and occupies a region significantly larger than the region in which the direct field is significant. In such configuration, the spatial integral and the summation in (6) can

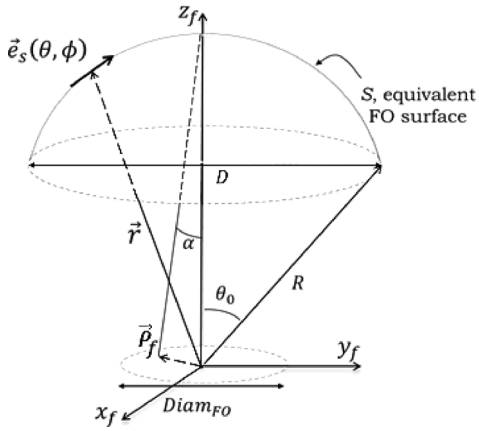

Fig. 3. Geometry of the equivalent FO surface of a generic focusing system.

be extended to infinity without making a significant error. The power can then be calculated resorting to the Parseval's Theorem, as follows:

$$P_{abs} \simeq \frac{R_s}{2w}\frac{1}{d_y}\frac{1}{4\pi^2}\int_{-\infty}^{\infty}\int_{\infty}^{\infty}\left|I_0\left(k_x,k_y\right)\right|^2 dk_x dk_y. \quad (7)$$

In this case the power is proportional to the incoherent weighed sum of the power associated to each plane wave separately. It is worth noting that, in all practical applications, since no evanescent waves reach the absorber surface, the integrals in (7) are spectrally limited. If one names $k_\rho = \sqrt{k_x^2+k_y^2}$, $k_{\rho 0} < k_0 \sin\theta_0$ defines such limit, where k_0 is the free space wavenumber and θ_0 is the subtended rim angle of the focusing system in Fig. 3. The integration domain can be further reduced when FO plane wave expansion is used as shown in the coming sections, where the coupling of a distributed absorber with a parabolic reflector and elliptical lens is investigated in detail by evaluating an analytical expression of the direct field plane wave spectrum.

III. FO Plane Wave Expansion

While for large F/D focusing systems, a plane wave spectrum can be simply evaluated, its evaluation is less obvious for small or moderate F/D. Rigorous procedures require the analysis of the field in the focusing system using adequate full wave techniques and then resorting to Fourier Transformations. Alternatively, an asymptotic procedure for the numerical evaluation of the PWS of the PO field of a reflector system was proposed by Pathak in [13]. In the optical domain, a technique much simpler than both these options is often used, namely the FO method, introduced by E. Wolf in [12]. FO calculates the PO currents in an equivalent sphere centered on the focal point, and exploits the approximation that the observation points are assumed at very large distance from the focalizing system in terms of the wavelength.

A. Spherical PWS

A vectorial FO representation of the electromagnetic field in a generic focusing system is presented in [12] and [14] and summarized in the Appendix, where its region of validity is also discussed. The electric field in the observation point, $\vec{\rho}_f = \rho_f \hat{\rho}_f$ (see Fig. 3), can be conveniently expressed as an integral over a sphere, with radius R and aperture diameter D, that subtends a rim angle θ_0, centered in the focus, as follows:

$$\vec{e}_f\left(\vec{\rho}_f\right) \approx \frac{jkRe^{-jkR}e^{-jk(\rho_f^2/2R)}}{2\pi}\int_{\Omega}\vec{e}_s\left(\theta,\phi\right)e^{jk\vec{\rho}_f\cdot\hat{r}}\sin\theta d\theta d\phi \quad (8)$$

where $\vec{r} = R\hat{r}$ represents a point over the spherical integration surface; Ω is the integration domain which is extended over the solid angle subtended by the focusing system (for the case of Fig. 3 $\theta \in (0,\theta_0)$, $\phi \in (0,2\pi)$); k is the propagation constant inside the focusing system medium (dielectric in the case of lenses), and $\vec{e}_s\left(\vec{r}\right) = \vec{e}_s(\theta,\phi)$ represents the electric field tangent to the equivalent sphere. This tangent field is the geometrical optics (GO) propagation of the field impinging on the focusing system (e.g., lens in Fig. 1) to the equivalent FO sphere. The explicit expression of $\vec{e}_s\left(\vec{r}\right)$ as a function of E_0^{PW}, amplitude of an external plane wave normally incident with respect to the focusing system, will be given in the following subsections for two cases of interest: parabolic reflector and elliptical dielectric lens.

In the Appendix, the domain of validity of the FO is discussed in detail since, to the best of our knowledge, such discussion is missing and it is significant at THz frequencies. It results that, for normal incidence, the FO applicability domain is defined by a circle in the focal plane (see Fig. 3) with diameter

$$Diam_{FO} = f_{\#}\min(0.4D, \sqrt{2f_{\#}D\lambda}), \quad (9)$$

where the integrand in (8) approximates the relevant PO integrand, (A.1), with an error smaller than 20% in amplitude or $\pi/8$ in phase. Note that $f_{\#} = R/D$.

If the quadratic term in front of the integral in (8) is neglected, the focal field is expressed as the sum of incremental contributions in which the observation point, $\vec{\rho}_f$, appears only at the exponent: i.e., the field is represented as a plane wave expansion. This approximation is clearly valid for absorbers placed close to the focal point.

B. Cylindrical PWS

An alternative representation in terms of cylindrical waves can be obtained by a simple change of variables. In fact, writing $k_\rho = k\sin\theta$ leads to $d\theta = dk_\rho/\sqrt{k^2-k_\rho^2}$ and, as a consequence

$$\vec{e}_f\left(\vec{\rho}_f\right) \approx \frac{jRe^{-jkR}}{2\pi}\int_0^{k_{\rho 0}}\int_0^{2\pi}\vec{e}_s\left(\sin^{-1}\left(\frac{k_\rho}{k}\right),\phi\right) \cdot \frac{e^{jk_\rho\rho_f\cos(\phi_f-\phi)}}{\sqrt{k^2-k_\rho^2}}k_\rho dk_\rho d\phi. \quad (10)$$

Accordingly, the cylindrical spectrum is limited to $k_\rho \in (0, k_{\rho 0})$.

C. Cartesian PWS

In some instances, a more standard Fourier transform representation may be convenient. This representation can be applied

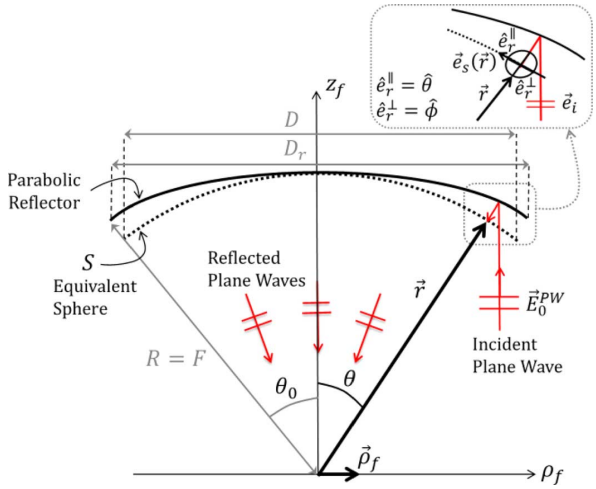

Fig. 4. Equivalent sphere and geometrical parameters for a parabolic reflector.

by using the following change of variable: $k_x = k_\rho \cos\phi$ and $k_y = k_\rho \sin\phi$:

$$\vec{e}_f(\vec{\rho}_f) \approx \frac{1}{4\pi^2}\int_{-\infty}^{\infty}\int_{-\infty}^{\infty}\vec{E}_f(k_x,k_y)\, e^{+jk_x x_f} e^{+jk_y y_f}\, dk_x dk_y \tag{11}$$

where $x_f = \rho_f \cos\phi_f$ and $y_f = \rho_f \sin\phi_f$ and

$$\vec{E}_f(k_x,k_y) = \frac{j2\pi R e^{-jkR}}{\sqrt{k^2-k_\rho^2}}\vec{e}_s\left(\sin^{-1}\left(\frac{k_\rho}{k}\right), \tan^{-1}\left(\frac{k_y}{k_x}\right)\right) \cdot circ(k_\rho, k_{\rho 0}). \tag{12}$$

IV. Canonical Geometries

In this section, we explicitly derive the expressions of the PWS for two canonical geometries: a parabolic reflector and an elliptical dielectric lens. We consider a plane wave incidence into these focusing systems from broadside with a linear polarization along x and an amplitude E_0^{PW}.

A. Parabolic Reflector

Fig. 4 shows the geometrical parameters together with the FO equivalent surface for a parabolic reflector. In this configuration, the equivalent surface, S, touches the reflector surface in the apex. Thus the sphere radius is equal to the focal distance, i.e., $R = F$. A parametrization of the integral in (8) in terms of (θ, ϕ) associates every point, $\vec{r}$, on the surface S to a ray with propagating vector $\widehat{k} = -\widehat{r}$, where $\widehat{r}$ is the radial unit vector. Each ray has undergone a reflection at the reflector's surface (see the inset of Fig. 4 for a visual clarification).

For a linearly polarized plane wave coming from broadside, the parallel and perpendicular unit vectors of the reflected fields coincide with the spherical unit vectors components, $\widehat{e}_r^{\parallel}(\theta,\phi) = \widehat{\theta}$ and $\widehat{e}_r^{\perp}(\theta,\phi) = \widehat{\phi}$. At S, the PO aperture field (i.e., the reflected field) is a local plane wave and its explicit expression becomes

$$\boldsymbol{\vec{e}_s(\theta,\phi) = -S_{pread}^{r}(\theta)\left(\cos\phi\widehat{\theta} - \sin\phi\widehat{\phi}\right)E_0^{PW}} \tag{13}$$

where the spreading term, $S_{pread}^{r} = 1/\cos^2(\theta/2)$, accounts for the conservation of energy in the ray path from the incidence plane to the reference sphere. The spreading term is calculated by imposing that the power density within the solid angle has to be equal to the power density reflected by the parabola. It is worth noting that the electric fields are all in phase at the equivalent sphere. The integral in (8) can be performed analytically for large R/D giving rise to the well-known Airy pattern, defined as

$$\vec{e}_f(\vec{\rho}_f) = -\frac{jkRe^{-jkR}}{2\pi}A(\rho_f)\,\widehat{x} \tag{14}$$

where $A(\rho_f) = (\pi D^2/2R^2)(J_1(k\rho_f D/(2R))/k\rho_f D/(2R))$.

In a general case, so when R/D is not too large, the integral along ϕ can be performed analytically using the integral representation of Bessel functions [14].

Finally, a Fourier transform representation of the focal field, (11), can be obtained by using the PWS for a normally illuminated parabolic reflector as

$$\boldsymbol{\vec{E}_f(k_x,k_y)} = -\frac{4\pi kRE_0^{PW}e^{-jkR}}{k_z}\frac{1}{k+k_z}\left(\frac{k_x}{k_\rho}\widehat{\theta} - \frac{k_y}{k_\rho}\widehat{\phi}\right)circ(k_\rho,k_{\rho 0}) \tag{15}$$

where $k_z = \sqrt{k^2-k_\rho^2}$.

Equation (8), with (13) and (15), highlights the representation of the field in the focal plane is represented as a sum of plane waves whose propagation directions are defined as those of the rays traveling from the reflector to the observation points. Accordingly, the PWS is limited to a spectral region defined by the parameterization of the reflector—$\theta \in (0, \theta_0)$. Fig. 5 shows the co-polar component of the electric field in the focal plane of a reflector characterized by $R/D = 3$ evaluated resorting to FO, a standard PO (GRASP software [15]) and the Airy pattern expression. For these large R/D cases, the focal fields resemble the Airy pattern. The results are presented for reflectors diameters of 20λ and 70λ,highlighting the respective FO domains of applicability. As it can be seen from Fig. 17(a) in the Appendix, the integrand is limited by an amplitude error for the small diameter, whereas by the phase error for the larger diameter. As observed in Fig. 5(a) (on the right), the limit of applicability for the smaller diameter indicates an error in the amplitude larger than 0.15 dB, whereas the phase has an error smaller than 12°. Instead, the amplitude error in the larger diameter is negligible (< 0.02 dB), whereas the phase error is larger than 25°. Therefore, the amplitude and phase applicability regions carried out for the argument of (A.3) are well translated in the same amplitude and phase applicability regions of the focal plane field.

B. Elliptical Dielectric Lens

A similar PWS spectrum can be obtained for an elliptical dielectric lens. Such lens has perfect focusing properties when its eccentricity is characterized by $e = 1/\sqrt{\varepsilon_r}$, with ε_r being the lens relative dielectric constant. Fig. 6 shows the lens geometry and the equivalent sphere, S, used for the FO calculation. Note that S touches the lens only in correspondence of its rim. Therefore, in this case, $R \neq F$.

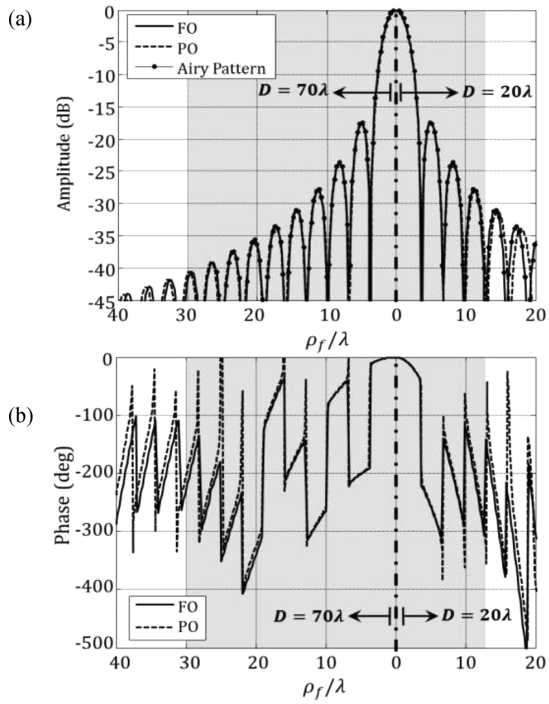

Fig. 5. Focal plane fields of $R/D = 3$ reflectors with two different diameters, $\boldsymbol{D = 20\lambda}$ (right side of the figures) and $\boldsymbol{D = 70\lambda}$ (left side of the figures), calculated using FO and compared with a normal PO (GRASP simulations) and with the well-known Airy pattern: (a) amplitude and (b) phase. The validity region is highlighted in grey. The fields are practically symmetric in $\boldsymbol{\phi}$ so only one of the main planes ($\boldsymbol{y = 0}$) are shown.

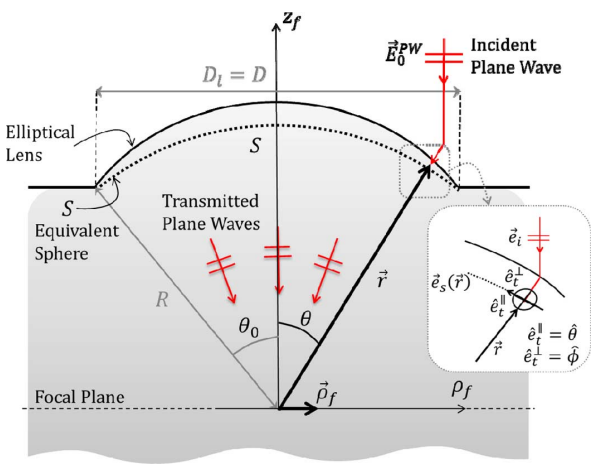

Fig. 6. Equivalent sphere and geometrical parameters for an elliptical lens.

The procedure to calculate the FO plane wave spectrum is analogous to the one described in the previous section, with the main difference being the expression for the field tangent to the sphere as follows:

$$\vec{e}_s(\theta,\phi) = S^l_{pread}(\theta)\left(\tau_{\parallel}(\theta)\cos\phi\widehat{\theta} - \tau_{\perp}(\theta)\sin\phi\widehat{\phi}\right)E_0^{PW} \tag{16}$$

where $\tau_{\parallel}(\theta)$ and $\tau_{\perp}(\theta)$ are the parallel and perpendicular transmission Fresnel coefficients. The transmission and reflection coefficients for a normally incident plane wave can be evaluated once it is recognized that the normal to the ellipse is

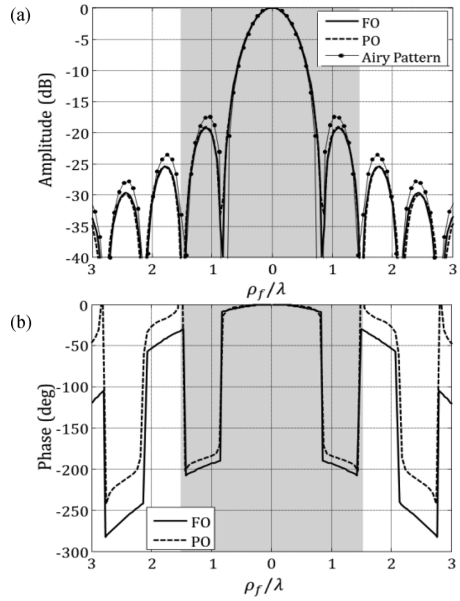

Fig. 7. Focal plane fields of an $R/D = 0.6$ elliptical silicon lens, with $D = 20\lambda = 6\lambda_0$, calculated using FO and compared with a normal PO and with the well-known Airy pattern: (a) amplitude and (b) phase. The validity region is highlighted in grey. The field is symmetric in ϕ so only one of the main planes ($y = 0$) are shown.

$\widehat{n} = \left((\cos\theta - e)\,\widehat{z} + \sin\theta\widehat{\rho}\right)/\sqrt{1 + e^2 - 2e\cos\theta}$. Moreover, the spreading function is calculated by imposing the power density within the solid angle has to be equal to the power density transmitted by the lens:

$$S^l_{pread}(\theta) = \frac{c\left(1-e^2\right)}{e\left(1 - e\cos\theta\right)}\frac{1}{R} \tag{17}$$

with c being half of the distance between the two foci of the ellipse. It is worth noting that when the eccentricity of the lens tends to zero the surface degenerate to a sphere, and $S^l_{pread}(\theta) = \sqrt{\cos\theta}$.

Therefore, the lens focal plane field can be approximated as a plane wave expansion, as in the previous section, using

$$\vec{E}_f(k_x,k_y) = \frac{j2\pi E_0^{PW}e^{-jkR}}{k_z}\frac{c\left(1-e^2\right)}{e\left(1-e\cos\theta\right)} \cdot\left(\tau_{\parallel}(\theta)\frac{k_x}{k_\rho}\widehat{\theta} - \tau_{\perp}(\theta)\frac{k_y}{k_\rho}\widehat{\phi}\right)\mathrm{circ}\left(k_\rho, k_{\rho 0}\right) \tag{18}$$

where $\theta = \sin^{-1}(k_\rho/k)$.

Fig. 7 shows the co-polar component of the electric fields in the focal plane of a $6\lambda_0$ diameter elliptical silicon ($\varepsilon_r = 11.9$) lens with $R/D = 0.6$ evaluated by resorting to FO, a standard PO, and the Airy pattern expression. As described by Fig. 17(b) in the Appendix, this case is limited by the phase error ($< 25°$). It is worth noting that for this small R/D case, the focal fields differ significantly from the Airy pattern. When the R/D of the lens decreases, the phase distribution changes over the surface and the uniform illumination condition, necessary for the Airy pattern to be formed, is not met any more. Indeed, when the R/D of the lens decreases, the field in the lens focal plane cannot be approximated any more by the Airy pattern [16]

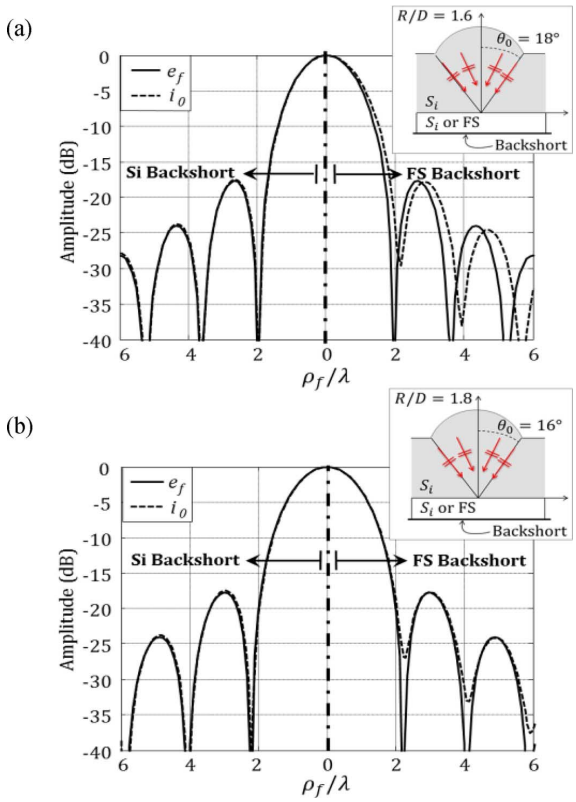

Fig. 8. Currents in the absorber central strip, at 250 GHz, for (a) $R/D = 1.6$ and (b) $R/D = 1.8$ silicon elliptical lenses with $D = 7.2$ mm. In both figures, the right side represents the backshort obtained via free space (FS) and, the left-hand side, obtained via a silicon slab. The normalized focal plane field is also shown. Absorber geometry: $d_y = 75$ μm and $w = 20$ μm, and sheet resistance $R_s = 30$ Ω. The insets show a drawing of the analyzed lens configuration.

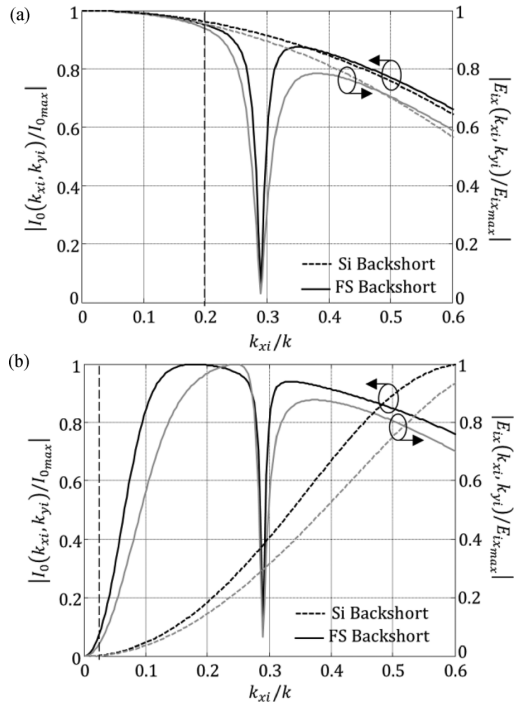

Fig. 9. Normalized current, black lines, and left axis, and normalized incident field, gray lines, and right axis, as a function of k_{xi}/k for $k_{yi} = 0$ for the same cases shown in Fig. 8. (a) $f = 250$ GHz and (b) $f = 500$ GHz.

V. Numerical Examples

In this section, we proceed to investigate the performance of distributed absorbers under focusing systems. Specifically, we start by observing the spatial current distribution on the strips when the absorber is located under a silicon elliptical lens. The separation layer between the absorber and the backing reflector is filled either via a silicon slab or a free space. The optimum absorber parameters are designed as explained in [10]. Fig. 8 shows the distribution of the current along the central strip calculated with (5) for two different R/D cases very close one to each other. Specifically, we assume D $= 20\lambda = 6\lambda_0$ and we consider $R/D = 1.6$ ($\theta_0 = 18°$) for the first case, while $R/D = 1.8$ ($\theta_0 = 16°$) for the second. For both cases, the observation ranges shown in Fig. 8 fall within the FO applicability region. The largest part of the power (95%) is contained within the main lobe and the first two secondary lobes. This is the most significant area when calculating the absorbed power. In the case of a reflector characterized by $R/D = 1.8$, the plane waves impinging on the absorber form, with respect to the focal plane normal (the z_f axis in Fig. 6), an angle smaller than the critical angle $\theta_c = 16.85°$ between silicon and free space. Conversely, for $R/D = 1.6$ ($\theta_0 = 18°$) the plane waves arriving to the absorber from the edge of the lens impinge with an angle larger than the critical angle. As can be observed from a comparison between Fig. 8(a) and (b), the two R/D produce appreciably different currents where free space backshort is present, despite the fact that they are associated to almost the same R/D (see the insets in Fig. 8). This difference is associated to the effect of the critical angle.

This effect can be appreciated thanks to the fact that the analytical tool presented here links the focusing system with the spectral Green's function of planar dielectric stratified media. To highlight this effect, Fig. 9 shows the variation of the spectral current, (3), normalized to its maximum value for the same two cases of Fig. 8 at two different frequencies. The peak around $k_{xi} = 0.29k$ is associated to the critical angle present only in the case of free space backshort. The effect of the critical angle is also present on the incident field, calculated in the absence of the absorber, as shown in the right axis of Fig. 9.

A. Proportionality Between Currents and Electric Field

Fig. 8(a) and (b) also shows the direct field coming from the focusing lens, normalized to its maximum value. In general, the shape of the spatial current differs from this field, since it depends on the integration of the spectral components of the direct field, the absorber equivalent circuit, and the effect of the dielectric stratifications on the incident field, as pointed in the previous section. However, a close observation of Fig. 8 suggests that, in some cases, the spatial distribution of the electric current and that of the focal direct field are essentially proportional one to the other, even for large ranges of observation. This occurs when the spectral variation of the current is small. Fig. 9(a) shows this variation for the same case than Fig. 8 at 250 GHz. One can see that the variation as a function of k_{xi}/k is constant up to an angle of about 10°, i.e., $k_{xi}/k \approx 0.2$. However, if we go to a different frequency, Fig. 9(b), the variation is constant only up to about 2°, i.e., $k_{xi}/k \approx 0.03$. Beyond these limits one cannot

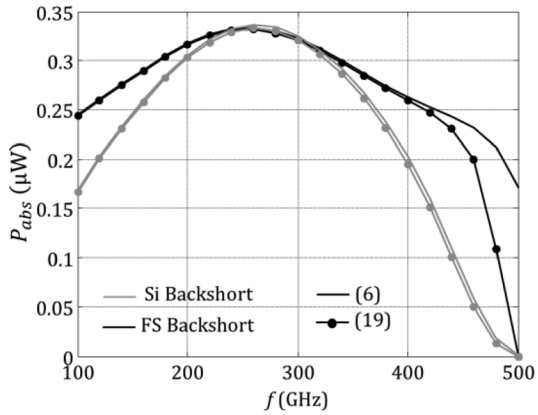

Fig. 10. Analytical absorption efficiency calculated for the same cases of Figs. 8 and 9, but using a lens with $\theta_0 = 10°$.

claim any sort of proportionality between the spatial current and direct fields without incurring in significant errors. In general, the limit will depend on the dielectric stratification in which the absorber is embedded and the frequency.

B. Simplified Model for Small Angular Regions

For cases with small variation of the direction of the incidence rays, it is useful to find a simplified expression to quantify the power absorbed using the previous proportionality between the currents and the direct field. To this regard, we can assume that $I_0\left(k_x, k_y\right) \approx I_0\left(0,0\right)$ in (5) and (6). Following several straightforward steps, one arrives to a simplified expression of the absorbed power:

$$P_{abs} = \frac{R_s}{2wd_y}\left|I_0\left(0,0\right)\right|^2 \frac{1}{4\pi^2}\iint_{Abs_{Area}} \left|A\left(\rho_f\right)\right|^2 dx_f dy_f \tag{19}$$

where $A\left(\rho_f\right)$ is defined in (14). The value of the spectral current at broadside, $I_0(0,0)$, can be evaluated in a generic dielectric stratification using (3), and it follows expression

$$\left|I_0\left(0,0\right)\right| = \left|\frac{E_f\left(0,0\right) S_{trat}}{Z\left(0,0\right) + \frac{R_s}{w}}\right| \tag{20}$$

where S_{trat} relates the incident voltage wave (V_{TM}^{+}) with the open circuit solution of the transmission line representation of the stratification at the absorber location (V_{TM} in [10]). Therefore, S_{trat} depends on the specific stratification where the absorber is embedded. In the cases of Figs. 8 and 9, $S_{trat} = 1 + \left(Z^d - Z^u\right)/\left(Z^d + Z^u\right)$ where Z^u and Z^d are the input impedances of the upper and lower half spaces defined in Fig. 2 evaluated at broadside (i.e., $Z^{u/d} = Z_{TE}^{u/d} = Z_{TM}^{u/d}$).

Therefore, the integration of the spatial current distribution in (5) can be simplified into a spatial integration over the well-known Airy pattern distribution, leading to a much faster computation time. Fig. 10 shows the calculated absorbed powers, using (6) and (19) for the same cases shown in Figs. 8 and 9, but using a lens with $\theta_0 = 10°$, as a function of the frequency. The agreement is very good except at the higher frequencies. For such frequencies, the proportionality between the spatial current and focal field is no more valid for the free space backshort. For this case, there is a significant variation of the spectral current in the angular range defined by the lens illumination (i.e., up to 10°) as shown in Fig. 9(b).

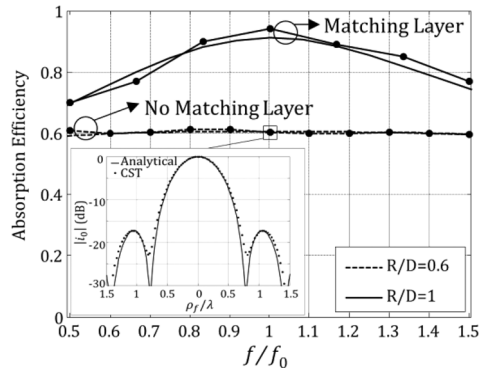

Fig. 11. Analytical absorption efficiency validated with CST (lines with dots) for two lenses: $R/D = 1$ (dashed lines), with matching layer, $d_y = 20$ μm, $w = 10$ μm and $R_s = 55$ Ω, and $R/D = 0.6$ (solid lines), without matching layer, $d_y = 75$ μm, $w = 20$ μm and $R_s = 30$ Ω. In both cases $D = 20\lambda = 6\lambda_0$ and a backshort in free space is used located at $\lambda_0/4$ at the $f = f_0$. The inset shows the current in the absorber validated with CST for the $R/D = 0.6$ case at the $f = f_0$.

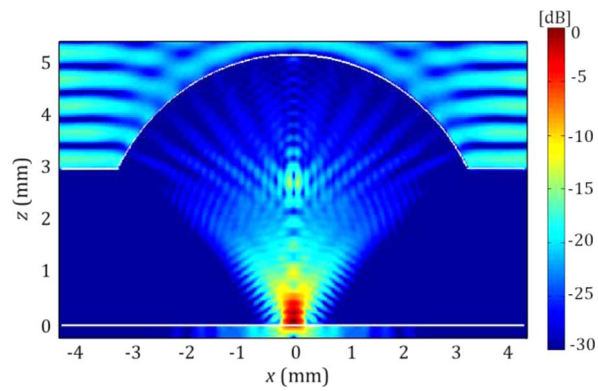

Fig. 12. Electric field amplitude for the $R/D = 0.6$ lens case shown in Fig. 9, at the central frequency.

C. Absorption Efficiency and Validation of the Model

In the general case, the absorption efficiency of a focusing absorbing system can be directly obtained using (6) and normalizing it by the power of the plane wave impinging on the focal system aperture (D_l in the case of the lens and D_r for the reflector) accordingly to Figs. 4 and 6. Fig. 11 shows this efficiency for a large $R/D = 1$ and a small $R/D = 0.6$ elliptical lenses. In the large R/D case the presence of a matching layer, with thickness $\lambda/4$ at the central frequency of the band, is included. The same cases have been analyzed by using the CST software for comparison; the excellent agreement is evident. The CST computation is very time consuming (for the cases shown in Fig. 11 CST took over two hours in comparison of the analytical method that took less than a minute). Moreover, the computation time in CST increases with the dimensions of the lens. This is because CST requires a full wave simulation of the whole optical system (Fig. 12 shows the electric field inside the lens simulated by CST for the same $R/D = 0.6$ case of Fig. 11). The inset of Fig. 11 shows the normalized current,

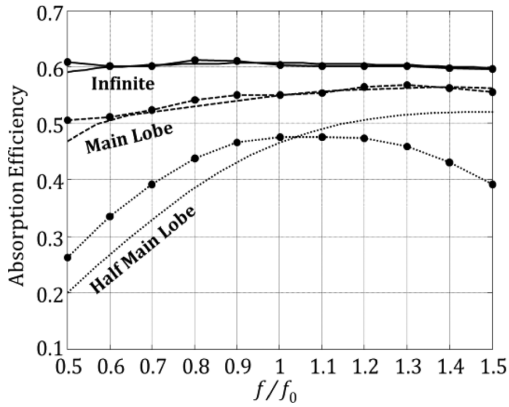

Fig. 13. Analytical absorption efficiency validated with CST (lines with dots) for three different areas of the absorber: infinite area and the areas which sample the main lobe and half of the main lobe, for the same $R/D = 0.6$ case of Fig. 11. Areas considered at the central frequency.

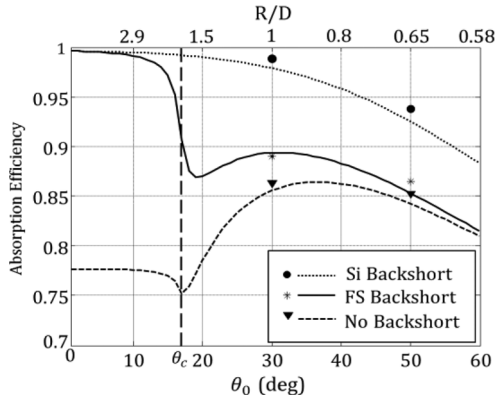

Fig. 14. Absorption efficiency versus lens subtended rim angle (the R/D value related to each angle is indicated in the upper axis) for three different stratifications: backshort in free space (FS) and using a silicon slab (in both cases $d_y = 53$ μm, $w = 14$ μm), and no backshort with free space under the absorber ($d_y = 41$ μm, $w = 14$ μm). In all cases, $\mathrm{D} = 70\lambda = 20\lambda_0$ (at $f_0 = 350$ GHz), $R_s = 30\ \Omega$ and a matching layer is used. Dots, asterisks and triangles correspond to CST simulations.

in the central strip of the absorber, validated with CST for the small R/D case at the central frequency.

To evaluate the current along the strips, the proposed model assumes an infinite extension of the absorber. A finite absorber dimension is only considering in the calculus of the absorbed power, (6). This is equivalent to neglect the edge effects associated to the absorber finiteness. However, these effects are usually very small, in practice, because of the significant loss in the metal strips. In order to study the validity of the approximation, Fig. 13 shows the absorption efficiency for different dimensions of the absorber, for the case $R/D = 0.6$ in Fig. 11, validated with CST. The absorber areas considered, apart from the infinite case, are those that sample the main lobe and half the main lobe of the field at the central frequency. It can be observed that the agreement is excellent except the smallest area. Indeed, this case has an absorber dimension of only 0.6λ at the central frequency and the truncation effect cannot be neglect. It is however to worth noting that the latter case is not a practical one and it is considered only for academic purposes. As a matter of fact, in common designs the absorber extends over a region larger than half a wavelength.

VI. Absorber Designs for KIDs

In this section, the proposed analytical model is used to design some absorber configurations with optimum performances. First, we point out the influence of different multilayer stratifications, placed at the focal plane of a dielectric lens, on the absorption efficiency. The efficiency of a free-standing absorber (an absorber placed on an infinite silicon medium) would have a maximum efficiency of 50% that would decay smoothly with the R/D ratio of the lens. To improve the efficiency, one can place a silicon backshort at $\lambda/4$. The efficiency goes up to 100% and also decays smoothly with the R/D ratio, as shown in Fig. 14. Instead, if the backshort is placed at $\lambda_0/4$ in free space, the efficiency will increase up to 100% but have unexpected variations versus the R/D ratio due to the presence of the critical angle, shown also in the same figure. The most surprising case is when the absorber is placed between infinite silicon and free space mediums. In this case the efficiency is 78% for normal incidence and increases for R/D ratios associated to subtended rim angles larger than the critical one, see Fig. 14. This increase is related to the fact that there is not power transmitted to the air medium after this angle. Fig. 14 also shows, for each case considered, the absorption efficiency calculated by using CST for the angles $\theta_0 = 30^\circ$ and $\theta_0 = 50^\circ$, as a further variation of the discovered trend.

Second, we have investigated how to maximize the absorption frequency bandwidth. According to Fig. 14, the optimum cases when a silicon/free space transition is present are: $\theta_0 = 13^\circ$ with backshort, where the efficiency starts to decrease after being approximately constant, and $\theta_0 = 35^\circ$ without backshort, where we have the maximum efficiency. The case where the backshort is in silicon is not considered here because, as it is proved in [10], it provides narrower bandwidth compare to the other cases considered. The efficiency as a function of the frequency is shown in Fig. 15, when a standard quarter wavelength matching layer is used. It is evident that the better performance, in terms of both efficiency and bandwidth, is obtained for the backshort case. The frequency response of this case is actually limited by the matching layer, and not by the absorber itself (see [10] for curves associated to plane wave efficiencies showing larger absorption bandwidths). If a double matching layer (or, for instance, wide-band grove based matching layers [17]) is employed, the efficiency bandwidths can be increased considerably as shown in Fig. 15.

Finally, a comparison of the efficiencies of KIDs coupled to reflectors versus lenses is presented in Fig. 16. Typically, reflectors are characterized by very large R/D ratios (e.g., future telescopes, as SPICA, are being planned with $R/D = 10$). In this case, the absorber is free-standing, i.e., printed in a very thin silicon membrane. Fig. 16 shows the efficiency of an infinite free-standing absorber under large R/D parabolic reflector, typical of space astronomical telescopes, for the SAFARI first frequency band. The 80% relative bandwidth corresponds to 1.4 octaves. In the same figure, the two best cases shown in Fig. 15 for the lens coupled absorbers are also plotted as reference. In these cases, the absorbers have a finite area that covers the first two secondary lobes of the focal field. The 80%

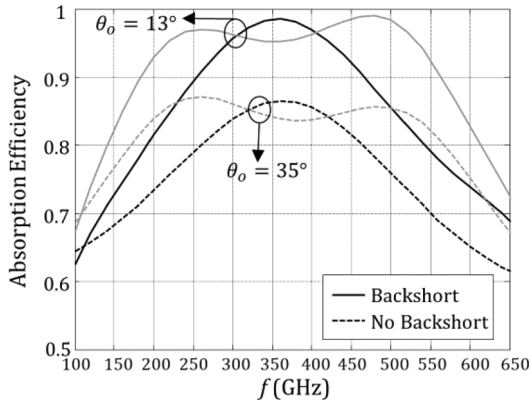

Fig. 15. Absorption efficiency for two optimized lenses with and without free space backshort. Black lines represent a single matching layer ($\varepsilon_{rm} = 3.45$ and $h_m = 115.4$ μm) and the gray lines a double matching layer ($\varepsilon_{rm1} = 2.07$, $\varepsilon_{rm2} = 4.90$, $h_{m1} = 144.1$ μm and $h_{m2} = 96.1$ μm). Same absorber parameters and lens aperture than in Fig. 14.

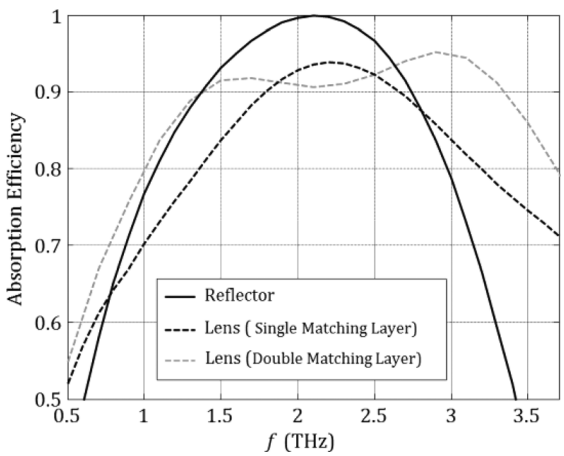

Fig. 16. Absorption efficiency optimized for SAFARI Scenario for a lens coupled absorber with $R/D = 2.2$ plus a free space backshort, and for a free-standing absorber printed on a thin silicon membrane of $\lambda_0/200$ thickness under a $R/D = 10$ reflector.

bandwidth of the single matching layer case is comparable to that of the parabolic reflector: 1.2 octaves. If a broader band matching layers is employed, the bandwidth can be significantly increased. For the example of the figure, the relative bandwidth is 1.9 octaves.

It could be possible to increase the absorption bandwidth also in absorbers on the focal plane of reflectors by using thick silicon substrates with broadband matching layers. However, for KID focal plane arrays, the absorbing area would be limited to at least 75% of the total array sampling area [5]. The remaining 25% area is required for the read-out circuits. Instead lens coupled KID will lead to a better sampling efficiency.

VII. Conclusion

KIDs present a promising alternative to the traditional bolometers for the new generation of THz cameras for Space. In a real scenario, absorber-based KIDs are located in the focal plane of focusing systems as reflectors or lenses. Coupling lenses characterized by small F/D ratios are typically used so the standard normal plane wave incidence analysis, used for large F/D systems, is not appropriate any more. Hence, the optimization of the absorber becomes a complex and time consuming task since it is done by means of full-wave analyses of the whole system. In this contribution, an analytical spectral model able to efficiently analyze THz absorbers distributed on the focal plane of focusing systems, having large or small F/D rations, has been presented. The model applies the Fourier optics plane wave representation of the focal plane fields to realistic reflector and lens systems linked to an analytical equivalent network, representing the absorber currents. Fourier optics approximations are usually applied in optical frequencies but the limits of validity are not established. In this paper, an effort has been made to clarify their region of applicability. Furthermore, a validation of the methodology via comparison with an alternative numerical full-wave technique has been presented. Finally, the method is used to derive some wide-band lens-coupled absorbers designs, obtaining high absorption efficiencies.

The method introduced in this paper is a powerful technique since simply links the spectral Green's function technique, useful for characterizing the field propagation in planar stratified media, with the focal fields in focusing systems. The whole method provides a better understanding of the physical insight of the problem, while providing an analytical tool for the characterization of the absorbers under focusing systems and avoiding time-consuming simulations. The development of the method has been initially driven by the analysis of absorber-based KIDs. However, it could be applied to other types of bolometric detectors, as well as it can be extended to the analysis of antenna coupled detectors.

Appendix
FO Applicability Region

In this appendix, the applicability region of the FO is described for a generic focusing system under plane wave incidence. The field radiated by any focusing system can be represented by equivalent currents distributed over an equivalent spherical surface S, of radius R, centered in the origin, see Fig. 3. Considering that there are no sources inside S, the focal electric field in $\vec{\rho}_f = (x_f, y_f)$ can be approximated as a radiation integral starting from the equivalent currents representation. Moreover, it can be demonstrated that if the plane wave impinges on the focusing system from broadside, the radiation integral can be expressed in terms of magnetic currents, $\vec{m}(\vec{r})$, only. In this situation the electric field along the focal region can be expressed as

$$\vec{e}_f\left(\vec{\rho}_f\right) = \int_s j\vec{k} \times \vec{m}\left(\vec{r}\right) \frac{e^{-jk\left|\vec{\rho}_f - \vec{r}\right|}}{4\pi\left|\vec{\rho}_f - \vec{r}\right|} d\vec{r} \qquad \text{(A.1)}$$

where $\vec{m}\left(\vec{r}\right) = 2\vec{e}_s\left(\vec{r}\right) \times \hat{n}$, $\hat{n} = -\hat{r}$, $\widehat{k} = (\vec{\rho}_f - \vec{r})/|\vec{\rho}_f - \vec{r}|$ and $\vec{e}_s$ is the PO aperture field. The actual expression of this field depends on the nature of the focusing system. A typical simplifying assumptions that is used in quasi optical systems, also in the microwave domain, is that the total field incident in the focusing system can be approximated using Geometrical optics. Thus, for each point on the equivalent sphere, Fig. 3, a ray is associated to the incident plane wave.

The radiation integral in (A.1) can be simplified by assuming that the radius R is the dominant distance in the amplitude. Thus, by using the standard phase approximations for the Fresnel region: $|\vec{\rho}_f - \vec{r}| \approx R - \vec{\rho}_f \cdot \widehat{r} + (\rho_f^2/2R)\left[1 - (\widehat{\rho}_f \cdot \widehat{r})^2\right]$, where $\vec{\rho}_f \cdot \widehat{r} = x_f \sin\theta\cos\phi + y_f \sin\theta\sin\phi$ and $\widehat{\rho}_f \cdot \widehat{r} = \cos\phi_f \sin\theta\cos\phi + \sin\phi_f \sin\theta\sin\phi$, (A.1) can be approximated as follows:

$$\vec{e}_f(\vec{\rho}_f) = \frac{jkRe^{-jkR}e^{-jk(\rho_f^2/2R)}}{4\pi} \int_\Omega \widehat{k} \times (\widehat{r} \times 2\vec{e}_s(\vec{r})) \times e^{jk\vec{\rho}_f \cdot \widehat{r}} e^{jk(\rho_f/2R)\sin^2\theta\cos^2(\phi_f - \phi)} d\Omega \quad \text{(A.2)}$$

where $d\Omega = \sin\theta d\theta d\phi$.

The integration appearing in (A.2) is relatively complex as both observation and source points are part of the integrand. The integral can further be simplified so as to obtain the FO representation, as follows:

$$\vec{e}_f(\vec{\rho}_f) = \frac{jkRe^{-jkR}e^{-jk(\rho_f^2/2R)}}{2\pi} \int_0^{2\pi}\int_0^{\theta_0} \vec{e}_s(\theta,\phi)\, e^{jk\vec{\rho}_f \cdot \widehat{r}} \sin\theta d\theta d\phi. \quad \text{(A.3)}$$

The following simplifying hypotheses have been made in order to arrive to (A.3)

$$A.\quad \widehat{k} = \frac{\vec{\rho}_f - \vec{r}}{|\vec{\rho}_f - \vec{r}|} \approx -\widehat{r}$$

$$B.\quad \frac{1}{|\vec{\rho}_f - \vec{r}|} \approx \frac{1}{R}$$

$$C.\quad e^{jk(\rho_f^2/2R)\sin^2\theta\cos^2(\phi_f - \phi)} \approx 1.$$

The points $\vec{\rho}_f$ in the focal plane where all three assumptions are verified will be indicated as the FO domain.

Approximation A simply corresponds to neglecting a field contribution that, relative to the one retained in the evaluation, is proportional to $\rho_f/R = \tan\alpha$. Here, α indicates the angle subtended from the focusing system to the observation point in the focal plane, see Fig. 3. Assuming that a 20% error on the field is tolerable, $\tan\alpha < 0.2$ corresponds to an angular limitation to $\alpha < 11^0$. Therefore, it is useful to define the diameter $Diam_{FO}^A = 0.4 f_\# D$ that limits the focal plane region, S_{FO}^A, where approximation A is valid. Accordingly, $\vec{\rho}_f \in S_{FO}^A$ corresponds to $|\vec{\rho}_f| < Diam_{FO}^A/2$.

Approximation B is standard in the evaluation of the far fields radiated by aperture distributions. A careful analysis leads to a 20% field error region defined by $Diam_{FO}^B = 0.8 f_\#^2 D$. This implies that $S_{FO}^A \in S_{FO}^B$, except for $f_\# \leq 0.5$. Thus in practice, this second condition can be neglected in all practical cases except for low frequency reflectors (typically used in radio astronomy).

A third domain of applicability of the FO, S_{FO}^C, emerges from approximation C. Imposing phase errors smaller than $\pi/8$, it results that $Diam_{FO}^C = f_\#^{3/2}\sqrt{2D\lambda}$. This condition has an explicit dependency on the wavelength and leads to the smallest domain for focusing system characterized by very large diameters since it does not grow linearly but with the square root of D. The overall applicability domain of the FO is the smallest of the three: $S_{FO} = \min(S_{FO}^A, S_{FO}^B, S_{FO}^C)$.

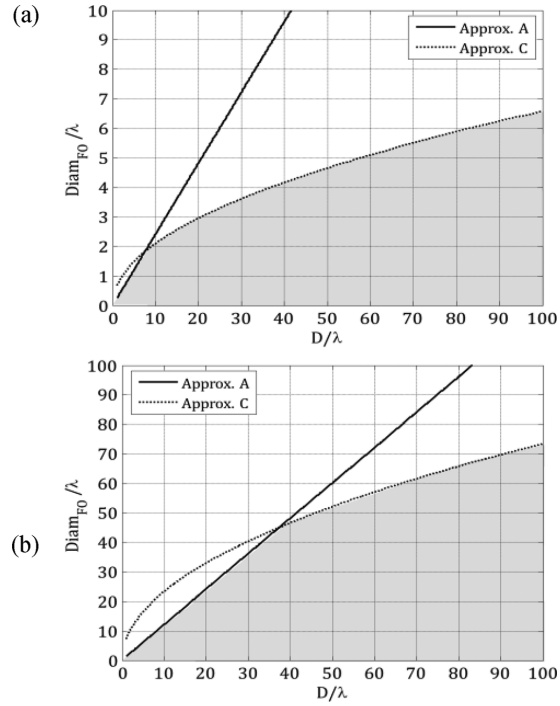

Fig. 17. Limits of applicability of the FO expression for (a) $R/D = 0.6$ and (b) $R/D = 3$. The gray area is the region where all the approximations are fulfilled.

Fig. 17 shows $Diam_{FO}^{A,C}$ for $R/D = 0.6$ and $R/D = 3$. For small diameters, approximation A is the most restricting one. This same approximation remains dominant also for relatively large diameters as the R/D number increases since the quadratic phase plays a smaller role. For large R/D and large diameters in terms of the wavelength (as in the optical domain), approximation C is the dominant one.

REFERENCES

[1] *Core Science Requirements for the European SPICA Instrument*, [Online]. Available: http://sci.esa.int/science-e/www/object/index.cfm?fobjectid=42283

[2] P. K. Day, H. G. Leduc, B. A. Mazin, A. Vayonakis, and J. Zmuidzinas, "A broadband superconducting detector suitable for use in large arrays," *Nature*, vol. 425, pp. 817–821, Oct. 2003.

[3] J. J. A. Baselmans, "Kinetic inductance detectors," *J. Low Temp. Phys.*, vol. 167, no. 3–4, pp. 292–304, May 2012.

[4] A. Baryshev *et al.*, "Large format antenna coupled microwave KID arrays for radioastronomy," presented at the IRMMW-THz, 2014.

[5] S. Doyle, P. Mauskopf, J. Naylon, A. Porch, and C. Duncombe, "Lumped element kinetic inductance detectors," *J. Low Temp. Phys.*, vol. 151, pp. 530–536, 2008.

[6] D. C. Araujo *et al.*, A LEKID-based CMB instrument design for large-scale observations in Greenland ArXiv, e-prints: 1407.6249, 2014 [Online]. Available: ArXiv.org

[7] C. M. McKennedy *et al.*, "Design considerations for a background limited 350 micron pixel array using lumped element superconducting microresonators," in *Proc. SPIE 8452, Millim., Submillim., and Far-Infrared Detectors and Instrumentation for Astronomy VI*, Sep. 2012, vol. 84520S.

[8] A. Baryshev, J. J. A. Baselmans, A. Freni, G. G. H. Hoevers, A. Iacono, and A. Neto, "Progress in antenna coupled kinetic inductance detectors," *IEEE Trans. THz Sci. Technol.*, vol. 1, no. 1, pp. 112–123, Sep. 2011.

[9] B. Blázquez, N. Llombart, A. Neto, and J. Bueno, "Development of lens-coupled LEKID detectors arrays for THz radiation," in *Proc. 6th Eur. Conf. on Antennas Propag.*, Mar. 2012, pp. 3264–3267.

[10] B. Blázquez, N. Llombart, D. Cavallo, A. Freni, and A. Neto, "A rigorous equivalent network for linearly polarized THz absorbers," *IEEE Trans. Antennas Propag.*, vol. 62, no. 10, pp. 5077–5088, Oct. 2014.
[11] J. Glenn *et al.*, "Numerical optimization of integrating cavities for diffraction-limited millimeter-wave bolometer arrays," *Appl. Opt.*, vol. 41, no. 1, pp. 136–142, Jan. 2002.
[12] E. Wolf, "Electromagnetic diffraction in optical systems. 1: An integral representation of the image field," *Proc. Roy. Soc. A*, vol. 253, pp. 349–357, 1959.
[13] A. Nagamune and P. Pathak, "An efficient plane wave spectral analysis to predict the focal region fileds of parabolic reflector antennas for small and wide angle scanning," *IEEE Trans. Antennas Propag.*, vol. 38, no. 11, pp. 1746–1756, Nov. 1990.
[14] L. Novotny and B. Hecht, *Principles of Nano-Optics*, 2nd ed. Cambridge, U.K.: Cambridge Univ. Press, 2012.
[15] "GRASP Software". TICRA, Copenhagen, Denmark.
[16] B. Richards and E. Wolf, "Electromagnetic diffraction in optical systems II. Structure of the image field in an aplanatic system," *Proc. Roy. Soc. London Ser. A*, vol. 253, pp. 358–379, 1959.
[17] A. Brahm *et al.*, "Laser-generated broadband antireflection structures for freeform silicon lenses at THz frequencies," presented at the IRMMW-THz, 2014.

Nuria Llombart (S'06–M'07–SM'13) received the Electrical Engineering and Ph.D. degrees from the Polytechnic University of Valencia, Valencia, Spain, in 2002 and 2006, respectively.

During her Master's degree studies, she spent one year at the Friedrich-Alexander University of Erlangen-Nuremberg, Germany, and worked at the Fraunhofer Institute for Integrated Circuits, Erlangen, Germany. From 2002 until 2007, she was with the Antenna Group at the TNO Defense, Security and Safety Institute, The Hague, The Netherlands, working as Ph.D. student and afterwards as researcher. From 2007 until 2010, she was a Post-Doctoral Fellow at the California Institute of Technology, Pasadena, CA, USA, working for the sub-millimeter Wave Advance Technology group of the Jet Propulsion Laboratory, Pasadena, CA, USA. She was a "Ramón y Cajal" fellowship at the Optics Department of the Complutense University of Madrid, Spain, from 2010 to 2012. Since September 2012, she is an Assistant Professor in the THz Sensing group at the Technical University of Delft, Delft, The Netherlands. She has co-authored over 100 journal and international conference contributions. Her research interests include the analysis and design of planar antennas, periodic structures, reflector antennas, lens antennas, and waveguide structures, with emphasis in the THz range.

Dr. Llombart was co-recipient of several NASA awards and of the H.A. Wheeler Award for the Best Applications Paper of 2008 in the IEEE TRANSACTIONS ON ANTENNAS AND PROPAGATION and the 2014 Best Paper Award in the IEEE TRANSACTIONS ON TERAHERTZ SCIENCE AND TECHNOLOGY. She received the 2014 IEEE Antenna and Propagation Society Lot Shafai Mid-Career Distinguished Achievement Award. She currently serves as Associated Editor for IEEE ANTENNAS AND PROPAGATION LETTERS and *IEEE Antennas and Propagation Magazine*. She also serves as Topical Editor for the IEEE TRANSACTIONS ON TERAHERTZ SCIENCE AND TECHNOLOGY and as a board member of the IRMMW-THz International Society.

Beatriz Blázquez received the B.Sc and M.Sc degrees in electrical engineering from Universidad Carlos III de Madrid, Madrid, Spain, in 2011, and is currently working towards the PhD. degree at the Terahertz Sensing Group, Technical University of Delft, Delft, The Netherlands.

From 2011 to 2012, she was working as a researcher at the Optics Department of the Universidad Complutense de Madrid, Madrid, Spain. Her research interests include reflector antennas, lenses, focal plane arrays and THz imaging applications.

Angelo Freni (S'90–M'91–SM'03) received the Laurea (Doctors) degree in Electronics Engineering from the University of Florence, Italy, in 1987.

Since 1990, he is with the Department of Electronic Engineering of the University of Florence, Italy, first as Assistant Professor and from 2002, as Associate Professor of electromagnetism. From 1995 to 1999 he has also been an Adjunct Professor at the University of Pisa, and from 2012 to 2014 a Visiting Professor at the TU Delft University of Technology, Delft, The Netherlands. During 1994, he was involved in research at the Engineering Department of the University of Cambridge, U.K., concerning the extension and the application of the finite element method to the electromagnetic scattering from periodic structures. Between 2009 and 2010, he also spent one year as a researcher at the TNO Defence, Security and Safety, The Hague, The Netherlands, working on the electromanetic modeling of kinetic inductance devices and their coupling with array of slots in THz range. His research interests include meteorological radar systems, radiowave propagation, numerical and asymptotic methods in electromagnetic scattering and antenna problems, electromagnetic interaction with moving media and remote sensing. In particular, part of his research concerned numerical techniques based on the integral-equation, with focus on domain-decomposition and fast solution methods.

Andrea Neto (M'00–SM'10) received the Laurea degree (*summa cum laude*) in electronic engineering from the University of Florence, Florence, Italy, in 1994, and the Ph.D. degree in electromagnetics from the University of Siena, Siena, Italy, in 2000. Part of his Ph.D. degree was developed at the European Space Agency Research and Technology Center, Noordwijk, The Netherlands, where he worked for the antenna section for over two years.

In 2000–2001, he was a Post-Doctoral Researcher at the California Institute of Technology, Pasadena, CA, USA, working for the sub-mm wave Advanced Technology Group. From 2002 to January 2010, was Senior Antenna Scientist at TNO Defence, Security, and Safety, The Hague, The Netherlands. In February 2010, he has been appointed Full Professor of Applied Electromagnetism at the EEMCS Department, Technical University of Delft, Delft, The Netherlands, where he formed and leads the THz Sensing Group. His research interests are in the analysis and design of antennas, with emphasis on arrays, dielectric lens antennas, wideband antennas, EBG structures, and THz antennas.

Dr. Neto was corecipient of the H. A. Wheeler award for the best applications paper of the year 2008 in the IEEE TRANSACTIONS ON ANTENNAS AND PROPAGATION. He was co-recipient of the best innovative paper prize at the 30th ESA Antenna Workshop in 2008. He was co-recipient of the best antenna theory paper prize at the European Conference on Antennas and Propagation (EuCAP) in 2010. He served as an Associate Editor of the IEEE TRANSACTIONS ON ANTENNAS AND PROPAGATION (2008–2013) and IEEE ANTENNAS AND WIRELESS PROPAGATION LETTERS (2005–2013). He is member of the Technical Board of the European School of Antennas and organizer of the course on Antenna Imaging Techniques. He is a member of the steering committee of the network of excellence NEWFOCUS, dedicated to focusing techniques in mm and sub-mm wave regimes. In 2011, he was awarded the European Research Council Starting Grant to perform research on Advanced Antenna Architectures for THz Sensing Systems. He is the Awards and Grants Chair for EUCAP 2014.